BioMedical Engineering OnLine

RESEARCH

Open Access

Discovery of potential ferroptosis and osteoporosis biomarkers through TMT proteomics and bioinformatics analysis

Hui Su[1†], Guoqing Tan[2†], WenXuan Guo[1,4], Jin Sheng Yu[1], Zhanwang Xu[2], RuJie Zhuang[1,3,4*] and Haipeng Xue[2*]

[†]Hui su and Guoqing Tan contributed equally to this work.

*Correspondence: rujiezhuang@163.com; 13287711511@163.com

[1] The First School of Clinical Medicine, Zhejiang Chinese Medical University, Hangzhou 310053, Zhejiang, China
[2] Department of Spine and Spinal Cord, Affiliated Hospital of Shandong University of Traditional Chinese Medicine, Jinan, 250000, Shandong, China
[3] Department of Orthopedics, Quzhou TCM Hospital at the Junction of Four Provinces Affiliated to Zhejiang Chinese Medical University, Quzhou 324002, Zhejiang, China
[4] Department of Traumatology and Orthopedics, The First Hospital Affiliated to Zhejiang Chinese Medical University, Hangzhou 310053, Zhejiang, China

Abstract

Background: Primary osteoporosis has increasingly emerged as a major issue affecting human health, with a complex specific pathogenic mechanism. As a research hotspot, ferroptosis plays a vital role in the pathogenesis of primary osteoporosis, aiming to explore the link and specific target genes between ferroptosis and primary osteoporosis.

Methods: By utilizing TMT proteomics and bioinformatics analyses, we elucidated the linkages and key targets of the ferroptosis pathway in an ovariectomized osteoporotic rat model. Forty 12-week-old SD female rats were employed in the study, of which 20 female SD rats were ovariectomized as the OVX group and 20 female SD rats were employed as the SHAM group. At the end of the experiments, the femurs of the rats were excised for computed tomography tests and used for hematoxylin and eosin staining. Finally, we extracted bone tissue proteins for TMT proteomics analysis and protein blotting verification.

Results: The proteomics results of the VX and SHAM groups showed that 133 proteins were significantly changed, of which 91 proteins were upregulated and 42 proteins were downregulated, including TXN, TMSB4X, TFRC, TF, RELA, PARP14, CP, CAPG, and ADIPOQ. The expression of key proteins in the bone tissues was detected by protein blotting. The expression of TFR1, TFRC and TF was upregulated, whereas the expression of Cp, TXN and BMP-2 was downregulated.

Conclusions: TMT proteomics and functional enrichment analyses in our study substantiated that in osteoporosis, disturbances in lipid metabolism lead to the emergence of oxidative stress with iron homeostasis imbalance.

Keywords: Potential biomarkers, Ferroptosis, Osteoporosis, TMT proteomics

Introduction

Primary osteoporosis (OP) is a systemic bone disease, which is characterized by destruction of bone microstructure leading to increased bone fragility and fracture risk. It represents a significant risk factor that threatens the lives and health of middle-aged and older adults [1]. Under normal conditions, bone formation and bone resorption are in dynamic balance. Nevertheless, following ageing and changes in estrogen levels,

insufficient bone formation is accompanied by increased bone resorption, leading to an imbalance in bone remodeling. This may result in decreased bone mass and bone strength, ultimately leading to osteoporosis and an increased risk of fracture. Osteoporosis is associated with high rates of disability and mortality [2]. In spite of the fact that the imbalance between bone resorption and bone formation due to various factors is considered to be the underlying cause of the pathogenesis of osteoporosis, the exact pathogenesis is still not completely clarified.

In 2012, Dixon [3] first characterized ferroptosis as an iron-ion-dependent form of non-apoptotic cell necrosis. This process is attributed to the abnormal metabolism of intracellular lipid peroxides catalyzed by iron ions, resulting in a dysregulation of iron ion homeostasis and inhibition of the activity of antioxidant proteins (e.g., GPX4). This may contribute to the production of large amounts of reactive oxygen species (ROS), which disrupts the intracellular redox balance and triggers cell death [4]. Recent studies have demonstrated that ferroptosis is strongly associated with a variety of diseases, including tumors, ischemia–reperfusion injury, and blood disorders [5]. Interestingly, there is growing evidence of an association between ferroptosis and osteoporosis [6, 7].

Iron is implicated in numerous bone metabolic pathways, regulating alkaline phosphatase activity as well as the expression of osteocalcin. Prior studies have demonstrated an inverse metabolic relationship between iron and calcium ions, where excessive iron accumulation can result in decreased bone mass and alterations in bone microarchitecture. The balance between osteoclasts, which mediate bone resorption, and osteoblasts, which are responsible for bone formation, directly influences the pathophysiology of bone tissue [8]. Ishii K has shown that iron overload generates substantial amounts of reactive oxygen species (ROS), thereby promoting osteoclast differentiation and accelerating bone resorption [9]. In Wang's experimental investigation [10], after culturing MC3T3-E1 cells in a high-glucose environment, it was established both in vivo and in vitro that ferroptosis plays a role in osteoclast differentiation during RANKL-induced differentiation. Additionally, the application of iron chelators was found to inhibit ferroptosis [11, 12]. Postmenopausal women often experience increased iron overload and oxidative stress, leading to diminished osteogenic activity and MSC osteogenic differentiation, while enhancing adipogenic differentiation, ultimately contributing to the development of osteoporosis.

TMT (tandem mass tag) technology serves as a labeling method for peptides in mass spectrometry analysis, enabling the comparison of protein expression profiles across diverse samples. However, its utilization within the realm of osteoporosis research remains limited. Existing studies have revealed a correlation between osteoporosis and iron overload in postmenopausal women, yet the underlying mechanisms remain elusive. To address this, we employed TMT proteomics in conjunction with bioinformatics to pinpoint crucial ferroptosis-related targets in a rat model of osteoporosis, with the ultimate goal of uncovering novel therapeutic strategies.

Results

Micro-CT measurements of rats

When compared to the rats in the SHAM group, a significant decrease in bone mineral density (BMD) was observed in the rats of the OVX group, with the difference being

statistically significant ($p < 0.01$). Analysis of femoral computed tomography (CT) scans of the rats revealed that the bone volume fraction (BV/TV), the bone surface-to-tissue volume ratio (BS/TV), and the trabecular bone number (Tb.N) were markedly lower in the OVX group ($p < 0.01$), whereas the trabecular separation (Tb.Sp) was notably higher ($p < 0.01$). These findings suggest considerable bone loss in the OVX group relative to the SHAM group. Statistical analysis further confirmed that the differences between the OVX and SHAM groups were statistically significant ($p < 0.05$) (Fig. 1).

Serum ELISA assay

In the OVX group, there was a significant reduction in the levels of bone morphogenetic protein-2 (BMP-2) and the osteogenic-specific transcription factor RUNX2, when compared to the SHAM group ($p < 0.01$). Additionally, an increase in serum transferrin receptor (TFR) and reactive oxygen species (ROS) levels was observed in the OVX group ($p < 0.01$). The results indicated that, within the osteoporosis model, there was an elevation in serum iron levels, accompanied by an increase in ROS and a decrease in serum osteogenic indices (Fig. 2A).

HE staining

When compared to the SHAM group, the bone trabeculae of the OVX group exhibited decreased density, widened intertrabecular spaces, thinning, fractures, sparse arrangement, a higher number of bone resorption lacunae, and a broader distribution.

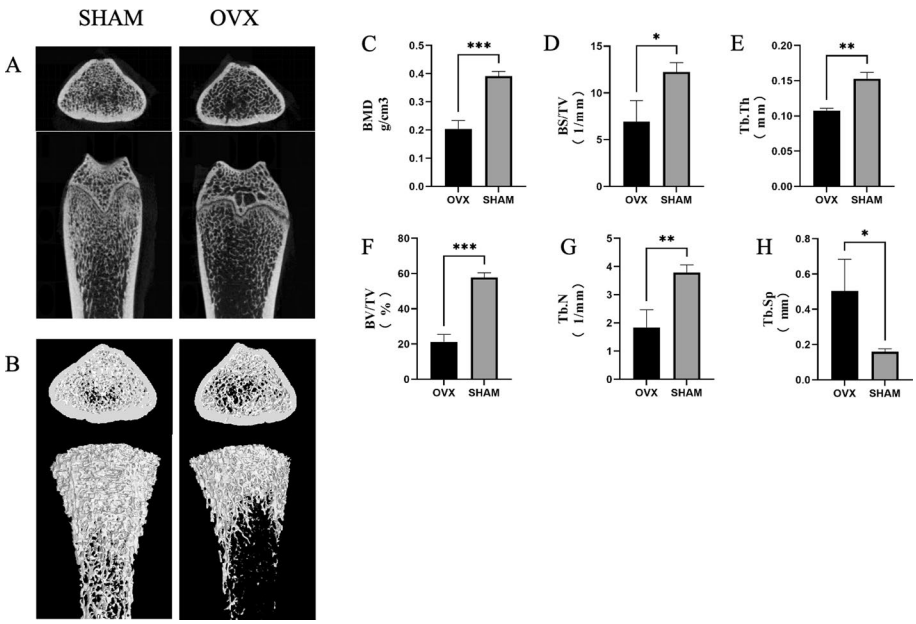

Fig. 1 Bone of micro-CT. **A**, **B** Micro-CT images of the femur. **C** BMD indicates the bone mineral density in the bone tissue of the region of interest. **D** Bone surface area and tissue volume ratio (BS/TV) can indirectly reflect the amount of bone mass. **E** Indicates the average thickness of the bone trabeculae. **F** Bone volume fraction (BV/TV) is commonly used in the evaluation of cortical and cancellous bone mass. **G** Number of trabecular bone (Tb.N) to evaluate the spatial morphological structure of trabecular bone. **H** Trabecular separation/spacing (Tb.Sp), the average width of the marrow cavity between the trabeculae. *$p < 0.05$, **$p < 0.01$, ***$p < 0.001$. Data were shown as mean ± SD, N = 20 per group

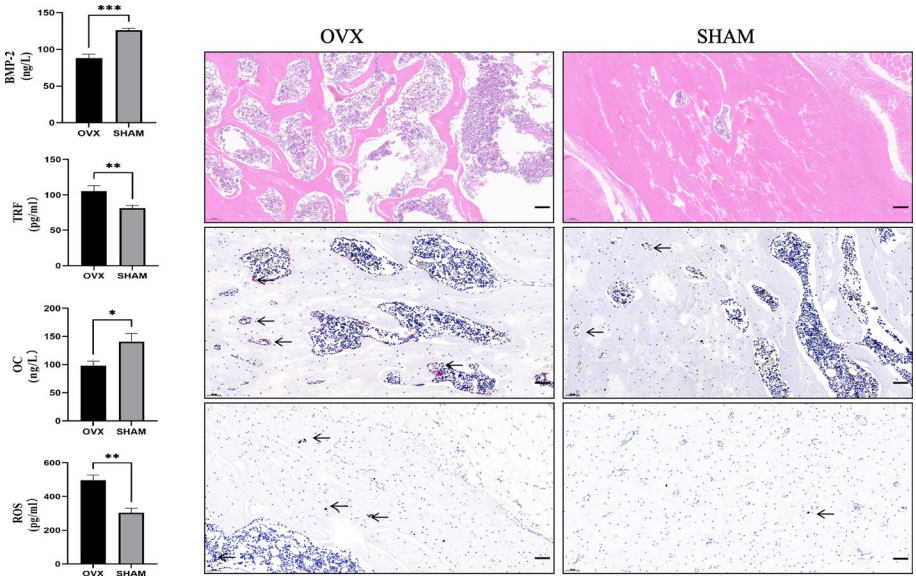

Fig. 2 Histobiochemical and pathological tests. **A** Serum ELISA assay, compared with SHAM group, *$p < 0.05$, **$p < 0.01$, ***$p < 0.001$, data were shown as mean ± SD, N = 20 per group; **B** H&E staining images of femur bone(→ mean the bone absorption hole)Scale bar100mm, 100x; **C** TRAP staining of femur bone(→ mean the Osteoclasts)Scale bar 50 mm.200x; **D** Prussian blue staining of femur bone(→ mean the Iron ion)Scale bar 50 mm.200x

In contrast, the bone trabeculae of the SHAM group demonstrated a normal count, good continuity, a uniform arrangement, and fewer bone resorption traps. These differing observations suggest that the bone trabeculae of the rats in the OVX group were in a poorer state and displayed apparent signs of osteoporosis (Fig. 2B).

TRAP staining

The results of tartrate-resistant acid phosphatase (TRAP) staining revealed that the osteoclasts were stained red. When compared to the SHAM group, the osteoclasts in the OVX group exhibited greater vigor and a wider distribution. Specifically, the number of osteoclasts was notably higher in the OVX group. These differing results indicated that osteoclast differentiation in the femoral tissue of rats in the OVX group was more pronounced than that in the SHAM group (Fig. 2C).

Prussian blue staining

Microscopic examination of the stained sections revealed a blue staining pattern corresponding to iron-containing heme or trivalent iron, and a red staining pattern for nuclei and other tissues. When compared to the SHAM group, the rats in the OVX group exhibited a more widespread distribution of the blue staining area. Conversely, the blue staining area in the SHAM group was less extensive and more scattered. These differing results suggest that the femur of the rats in the OVX group contains a higher concentration of iron ions compared to the SHAM group (Fig. 2D).

TMT quantitative proteomics of the DEPs between the OVX and the SHAM

After a duration of 12 weeks, bone tissues collected from each group were subjected to TMT quantitative proteomics analysis. The results obtained demonstrated that the effective spectral count was 41,881, with a total of 29,979 peptides and 3,424 proteins identified. When comparing the OVX group to the SHAM group, 3,055 proteins were identified. A p-value threshold of ≤ 0.05 and a fold change of 1.2 were utilized as criteria to screen for differential proteins (Fig. 3). The analysis revealed that 133 proteins exhibited significant differential expression (Table 1), among which 91 proteins were upregulated and 42 were downregulated (Fig. 2D).

Cross-tabulation analysis of DEGs and ferroptosis-related genes

The 133 DEGs and ferroptosis-related genes (from FerrDb database, http://www.zhounan.org/ferrdb/index.html) were intersected, and 9 DEGs were found to be ferroptosis-regulated genes, namely TXN, TMSB4X, TFRC, TF, RELA, PARP14, CP, CAPG, and ADIPOQ. (Fig. 4A, B).

Enrichment of KEGG pathway analysis

We conducted a KEGG pathway analysis on the 133 differentially expressed genes (DEGs) identified between OVX and SHAM rats. The analysis revealed that these DEGs were notably enriched in pathways such as thermogenesis, the RIG-I-like receptor signaling pathway, ferroptosis, the PPAR signaling pathway, and oxidative phosphorylation. These findings underscore the activation of the oxidative stress system and the implication of ferroptosis in the pathophysiology of osteoporotic rats. Furthermore, they

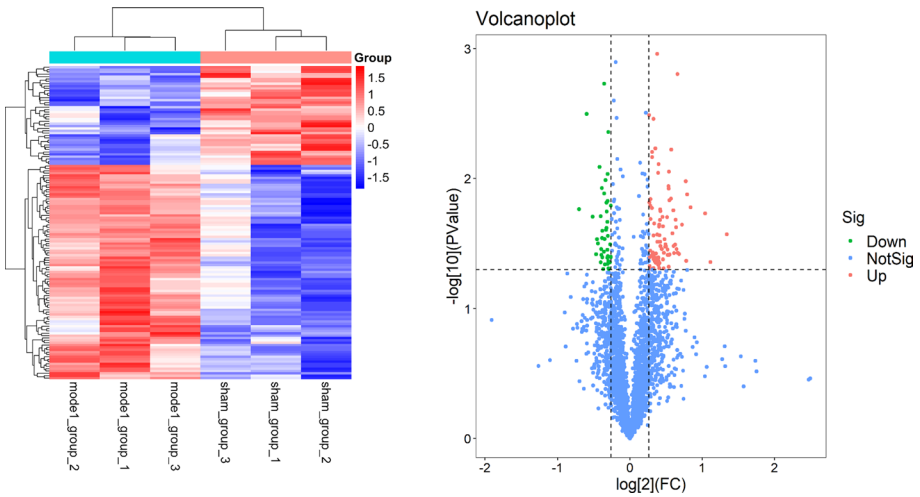

Fig. 3 Differential gene heat map and volcano map. The left panel is a heatmap showing the differential protein expression between the OVX and SHAM groups. Red for upregulation, blue for downregulation, and white for no significant change. OVX group samples (model group) are primarily on the right, showing more red (upregulated proteins), while SHAM group samples are on the left, showing more blue (downregulated proteins).The right panel is a volcano plot displaying differential protein expression. The x-axis represents log2 fold change (log2(FC)), and the y-axis represents -log10(P-value). Each point represents a protein: red for significantly upregulated proteins (log2(FC) > 1.2, $P \leq 0.05$), green for significantly downregulated proteins (log2(FC) < −1.2, $P \leq 0.05$), and blue for non-significant changes ($P > 0.05$). Most proteins show no significant change (blue points), with some significantly upregulated (red points) or downregulated (green points) in the OVX group

Table 1 133 significantly DEGs in SHMA group vs OVX group

Gene Name	FC(OVX group *vs* SHAM group)	pValue(OVX group *vs* SHAM group)	Sig(OVX group *vs* SHAM group)
UN	0.729437	0.02936	-1
Nop16	1.734694	0.013278	1
Ewsr1	1.315442	0.043073	1
Tf	1.716839	0.042932	1
UN	2.532258	0.026925	1
Bod1l1	1.562176	0.034977	1
Cdc5l	1.540925	0.032347	1
Rbmxrtl	1.323258	0.048795	1
Rbp4	1.554494	0.023768	1
Lxn	1.31297	0.046108	1
Pltp	0.808627	0.045395	− 1
Pon1	0.755433	0.019534	− 1
Trim25	1.308264	0.009069	1
Erlec1	1.244211	0.037244	1
Mbnl1	1.335469	0.017346	1
Ndufa5	0.661242	0.003189	− 1
Wdr77	1.25308	0.038591	1
Nans	1.214771	0.049083	1
Hnrnpa3	1.602548	0.038249	1
Cp	0.784159	0.029239	− 1
Dstn	1.434901	0.0389	1
Slc4a1	0.700057	0.019709	− 1
Pspc1	1.334278	0.020871	1
Tardbp	1.253315	0.048896	1
Tnpo1	0.805169	0.040704	− 1
Ddah2	1.204469	0.01529	1
Crip1	2.060599	0.018567	1
Sfr1	1.336674	0.030738	1
Txn	1.517429	0.033171	1
Cmpk1	1.296887	0.026995	1
Rasl12	0.781183	0.001863	− 1
Tubg2	0.794996	0.024898	− 1
Tes	1.380285	0.048977	1
Nup98	1.3729	0.023342	1
Thbs1	0.813675	0.043066	− 1
Sf3a2	1.426039	0.019862	1
Rap1b	0.798283	0.015389	− 1
UN	1.321781	0.023508	1
Mad1l1	1.35601	0.035005	1
Sh3bp1	1.216314	0.036084	1
Czib	1.220839	0.039422	1
Bclaf1	1.327899	0.044498	1
Rpl26	1.305159	0.044194	1
Sept7	1.434809	0.035297	1
A1m	0.767489	0.025307	− 1
Ssb	1.217253	0.020513	1
Tfrc	0.781025	0.013045	− 1
Afm	0.765548	0.028793	− 1

Table 1 (continued)

Gene Name	FC(OVX group *vs* SHAM group)	pValue(OVX group *vs* SHAM group)	Sig(OVX group *vs* SHAM group)
Tpr	1.282581	0.037826	1
Ptprd	1.283802	0.041043	1
Gsr	1.337872	0.033111	1
Sh3gl1	1.516189	0.017608	1
Cox6c2	0.808489	0.009235	− 1
Ccdc25	1.364407	0.019828	1
Septin11	1.314118	0.00776	1
Serpina1	0.792492	0.01031	− 1
Hsp90b1	0.828277	0.032223	− 1
Phf5a	1.462836	0.038455	1
Capg	1.210471	0.040032	1
Mmp2	1.451565	0.038787	1
Bphl	0.808261	0.014949	− 1
Padi2	0.832337	0.04018	− 1
LOC100911422	1.25444	0.040842	1
Grhpr	0.832618	0.016189	− 1
Lgals1	1.261738	0.038504	1
UN	1.254059	0.027541	1
Rela	1.64761	0.022684	1
Gpsm1	0.768367	0.040347	− 1
Prkar2b	1.24681	0.037888	1
Gsta6	1.237684	0.006249	1
Tmem38a	0.814663	0.049048	− 1
Tmsb4x	1.525125	0.037602	1
Cbx3	1.394099	0.029373	1
Cd2ap	1.313012	0.0407	1
Cd55	1.237348	0.006864	1
Bpgm	0.809929	0.027734	− 1
Rabggta	0.825034	0.044064	− 1
Fabp5	1.577138	0.001571	1
Pin1	1.483352	0.014323	1
Apool	0.775307	0.049558	− 1
LOC103690005	1.207898	0.046968	1
Pdgfrl	1.445898	0.011485	1
St13	1.24443	0.037942	1
Nup54	1.214048	0.01618	1
Coq6	0.805292	0.021598	− 1
Lima1	1.371038	0.041842	1
LOC102553715	1.201085	0.003256	1
Ndufv3	1.274161	0.043419	1
Ahnak	1.262833	0.022234	1
Csrp2	1.789913	0.016687	1
Ikbip	1.459828	0.014734	1
Sh3kbp1	1.41256	0.033277	1
Cops2	0.800314	0.017957	− 1
Unc45b	0.785949	0.045614	− 1
Hnrnpdl	1.402476	0.033566	1
Arl8b	0.816894	0.049672	− 1

Table 1 (continued)

Gene Name	FC(OVX group *vs* SHAM group)	pValue(OVX group *vs* SHAM group)	Sig(OVX group *vs* SHAM group)
UN	1.281094	0.044301	1
Tax1bp3	1.384259	0.037451	1
Sorbs1	1.299594	0.03081	1
Lmna	1.448111	0.011984	1
Zfand6	1.483871	0.006006	1
Eea1	1.301431	0.04232	1
Slc9a3r2	1.3274	0.027415	1
Cyc1	0.748503	0.008173	− 1
Lims1	1.581095	0.037446	1
Uaca	1.254296	0.003475	1
Dmd	0.799302	0.02408	− 1
Atp2a2	0.764471	0.011849	− 1
Cald1	1.32434	0.022732	1
Ppp1r12b	1.500076	0.026439	1
Sorbs3	1.216952	0.014434	1
Ndufa4	0.760897	0.038884	− 1
Erc1	1.233038	0.016883	1
Dbi	1.452124	0.008877	1
Fhl1	1.266131	0.04316	1
Luzp1	1.70905	0.010519	1
Eif3b	0.809993	0.039681	− 1
Hba-a3	0.780429	0.036699	− 1
Parp14	0.805203	0.035471	− 1
Spag7	1.276588	0.005876	1
Adipoq	1.451087	0.047528	1
Golga3	1.338026	0.017874	1
Pqbp1	1.548423	0.020767	1
Atp5mf	0.756763	0.044032	− 1
Filip1l	1.299449	0.001099	1
Sh3bgrl	1.405624	0.032145	1
Vars2	1.253941	0.041459	1
Nqo2	2.164036	0.043784	1
Ndufb9	0.735895	0.031616	− 1
Usp47	0.723794	0.038398	− 1
Fundc2	0.613812	0.01728	− 1
Golph3l	0.814029	0.004388	− 1
Pex14	0.759324	0.034964	− 1

133 proteins were identified in the comparison between the OVX and the SHAM groups, p-value ≤ 0.05, $N = 3$ per group. Fold change 1.2 times were used to screen the differential proteins

indicate the involvement of lipid metabolism regulation, particularly through the PPAR signaling pathway (Fig. 4C).

Enrichment of Gene Ontology (GO) analysis

A Gene Ontology (GO) analysis was conducted on the 133 differentially expressed genes (DEGs) identified between the OVX and SHAM groups, and the results were subsequently visualized. The top 20 GO terms, ranked by their enrichment scores, were

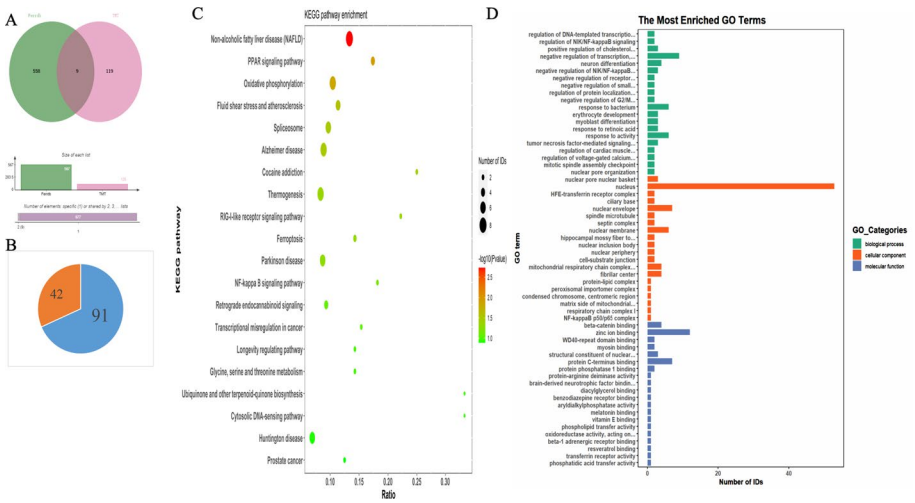

Fig. 4 Bioinformatics analysis of differential genes. **A** Venn diagram of DEGs the comparison of gene expression in the TMT proteomics and the Ferrdb database. The sum of the numbers in each circle represents the total number of DEGs for the comparison combination, and the overlapping part of the circle represents the DEGs shared between the two comparison groups. **B** pie diagram of DEGs: the abscissa represents the comparison group for the difference analysis, the ordinate indicates the number of difference genes, the color indicates regulation. Blue = up, orange = down. **C** enrichment analysis of the DEGs: top 20 of KEGG pathway analysis of DEGs. **D** Top 20 of Gene Ontology (GO) analysis of DEGs including biological processes(BP), cell component (CC), and molecular function (MF)

selected for further consideration. These terms encompassed 4 biological processes (BP), 13 cellular components (CC), and 3 molecular functions (MF). Among the CCs, notable enrichments were observed in the nuclear envelope, the HFE-transferrin receptor complex, the nuclear periphery, mitochondrial respiratory chain complex I, the nuclear pore nuclear basket, and other related structures. Based on the analysis outcomes, we noted alterations in the mitochondrial and nuclear membranes of osteoporotic rats. These changes were accompanied by the regulation of iron regulatory genes (Fig. 4D).

PPI network analysis

The PPI network of 133 DEGs were constructed by STRING (https://cn.string-db.org/), and the analysis resulted in 128 nodes, and 141 edges and the average node degree was 2.2. A total of 129 proteins interacted individually or through various interactions, among which Cdc5l, Ndufa4, Serpina1, Cox6c, Cyc1, Hsp90b1, Pon1, and Tardbp exhibited strong correlations. Additionally, we identified that ferroptosis-related genes, including TXN, TMSB4X, TFRC, TF, RELA, PARP14, and CP, displayed varying degrees of correlation. Notably, the interaction between Txn1, Cp, and Tfrc was more pronounced (Fig. 5). Furthermore, we constructed differential protein–protein interaction (PPI) network maps. The biological processes that demonstrated strong correlations included negative regulation of N/F-kappa B signaling, positive regulation of bone resorption, acute-phase response, negative regulation of intracellular protein transport, regulation of interleukin-8 production, and iron ion transport. The cellular components were primarily enriched within the HFE-transferrin receptor complex. Among the identified pathways, we observed that, in addition to the ferroptosis pathway, the HIF-1 signaling pathway, and the longevity regulating pathway, the more pertinent KEGG pathways

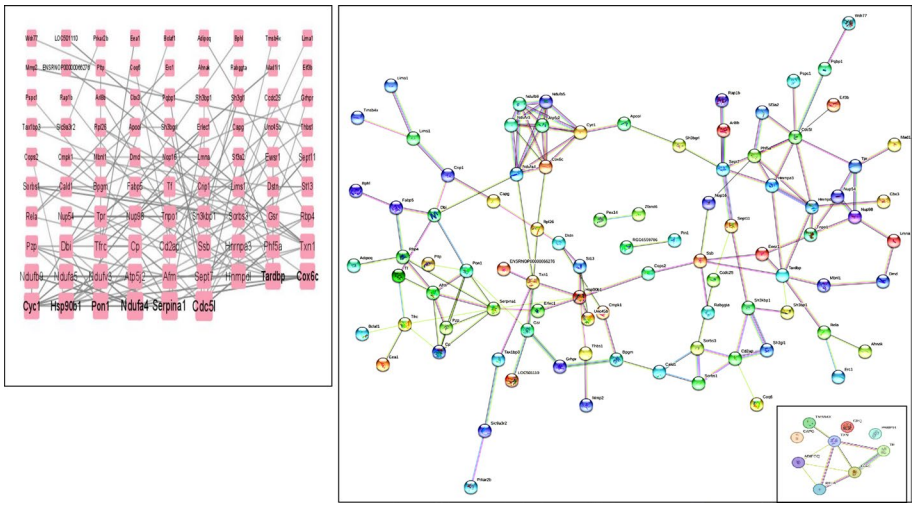

Fig. 5 PPI networks of DEPs. **A** TRING data base. **B** Cytoscape

were also involved in adipocytokine signaling. Analysis using wikipathway revealed a robust correlation between glutathione and NADPH, hinting at the regulation of our oxidative stress system with respect to NADPH production. Consequently, the analysis indicated that in the rat model of osteoporosis, pathways related to bone metabolism, such as bone resorption and bone formation, were altered. Furthermore, there was a close interplay among three pathways: lipid metabolism, which includes lipid regulatory genes, Ferroptosis, and the aforementioned bone metabolic pathways.

Validation of proteomics results

Through Western blotting analysis, we observed that the expression levels of TFR1, TFRC, and TF were upregulated in bone tissues. Conversely, the expression levels of Cp, TXN1, and BMP-2 were significantly downregulated in bone tissues. These findings were in agreement with the results obtained from the proteomics analysis. The differences observed were statistically significant when compared to the Sham group ($p < 0.05$) (Fig. 6).

Discussion

Primary osteoporosis is characterized by an imbalance between bone resorption and bone formation [13]. Currently, there is a growing body of research focusing on the relationship between ferroptosis and osteoporosis [14]. It is well-established that both iron deficiency and iron overload can contribute to the development of osteoporosis. Ferroptosis, a form of cell death characterized by iron-dependent lipid peroxidation, plays a pivotal role in this process [15] (Fig. 7). The accumulation of iron ions leads to mitochondrial dysfunction, disrupting lipid homeostasis and triggering lipid peroxidation. This, in turn, results in the production of large amounts of reactive oxygen species (ROS), which exert a negative regulatory effect on bone metabolism. Iron is an essential ion for the mitochondrial oxidative respiratory chain, and mitochondria, which are rich in iron, are considered to be key sites for ROS production and the occurrence of ferroptosis [16]. In our experiments, we observed significant regulation of differential genes in various

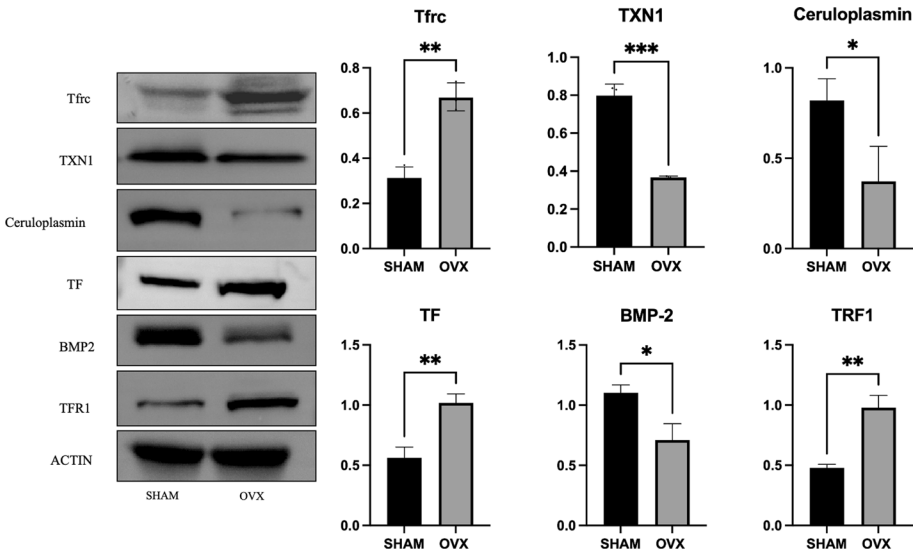

Fig. 6 Expression levels of the related proteins compared with SHAM group, $*p < 0.05$, $**p < 0.01$, $***p < 0.001$. Data were shown as mean ± SD, N = 3 per group

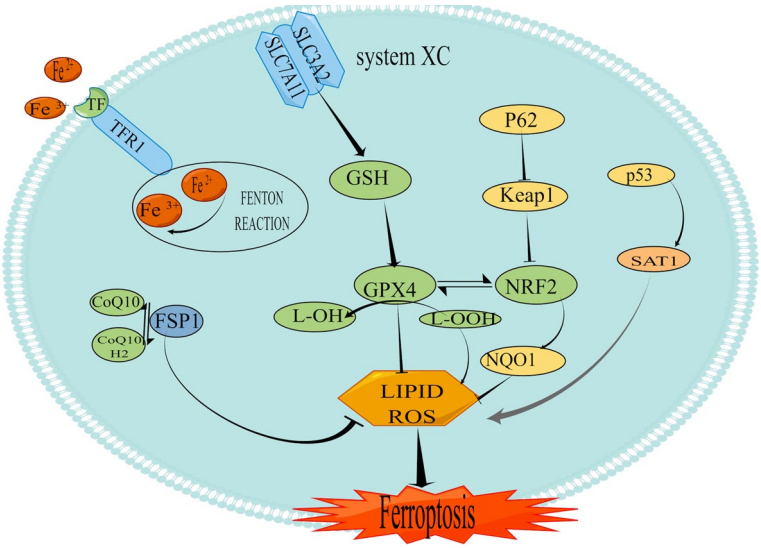

Fig. 7 Signaling pathway diagram of ferroptosis

nucleus-related structures and functions, including the nuclear pore, nuclear envelope, mitochondrial respiratory chain complex I, nuclear inclusion body, and nuclear periphery. Additionally, there was regulation involving bone resorption, iron ion transport, osteoclast differentiation, the HFE-transferrin receptor complex, and other pathways related to iron regulation and bone metabolism. These findings suggest that ferroptosis manifests in the morphology and function of cells in osteoporosis. Specifically, mitochondria exhibited morphological alterations, with wrinkled mitochondrial membranes, reduced or absent mitochondrial cristae, and fragmented outer membranes [17].

In our study aimed at verifying the role of the ferroptosis pathway in regulating osteoporosis, we identified the involvement of both the PPAR signaling pathway and the

adipocytokine signaling pathway. The PPAR signaling pathway is known to regulate lipid metabolism and glucose homeostasis, and it possesses the capacity to promote adipocyte differentiation [18]. Specifically, the activation of the PPAR signaling pathway in bone metabolism promotes lipogenic differentiation while inhibiting osteogenic expression [19, 20]. These findings suggest that the PPAR signaling pathway and the adipocytokine signaling pathway may serve as key pathways in the pathophysiology of osteoporosis. Among the adipokines, ADIPOQ stands out as the most active one, influencing lipid and carbohydrate metabolism and playing a crucial role in adipogenesis. Furthermore, ADIPOQ plays a significant part in regulating bone metabolism by inhibiting osteogenic protein expression and promoting osteoclast differentiation [21]. Our proteomic analysis revealed that Adipoq and RELA were significantly upregulated in osteoporotic rats, suggesting their importance in lipid metabolism through the PPAR signaling pathway and the adipocytokine signaling pathway. RELA is a key regulator of the NF-κB signaling pathway. Yu et al. [22] found that the deletion of RELA enhanced the osteogenic differentiation ability and adipose differentiation of mesenchymal stem cells (MSCs). Moreover, the activation of the NF-κB regulatory system promotes excessive mitochondrial autophagy in adipocytes, thereby inhibiting adipogenesis [23].

Studies have consistently shown that bone loss is often accompanied by oxidative stress [24]. Our current research [25] has further revealed that oxidative stress impairs the function of the Wnt/β-catenin signaling pathway in regulating bone remodeling. As a crucial regulatory system in oxidative stress, the relationship between glutathione and NADPH is indispensable for maintaining cellular redox homeostasis and regulating cellular metabolism [26]. Ferroptosis is characterized by the excessive production of reactive oxygen species (ROS) and the depletion of intracellular glutathione (GSH), ultimately leading to the inactivation of glutathione peroxidase 4 (GPX4). This, in turn, results in the accumulation of lipid peroxidation, which is pivotal for cell survival and serves as the core regulatory protein in ferroptosis [27, 28]. The significance of the relationship between glutathione and NADPH was corroborated by the data obtained from our experimental analysis. Furthermore, the present analysis also confirmed the involvement of the HIF-1 signaling pathway and the Longevity regulating pathway in the regulation of the oxidative stress system. HIF-1 has been implicated in vascular remodeling and generation, redox homeostasis, as well as glucose metabolism [29]. Additionally, oxidative stress, inflammation, and hypoxia induce the expression of HIF, which plays pivotal roles in regulating osteoclast-mediated bone resorption, osteoblast cellular bone formation, and angiogenesis [30].

Transferrin (TF) is a pivotal regulatory protein in maintaining iron homeostasis [31]. TFRC (also known as TFR1) and TFR2 are two isoforms of the transferrin receptor that bind to the iron–transferrin complex, facilitating the entry of iron into cells [32]. Our current study has uncovered that the expression of TFRC is upregulated during ferroptosis, resulting in excessive iron uptake by cells [33]. This, in turn, leads to an overproduction of reactive oxygen species (ROS) and disrupts the homeostasis of bone metabolism [34, 35]. Ceruloplasmin (Cp) functions as a plasma oxidase, capable of oxidizing Fe^{2+} to Fe^{3+}, allowing it to bind to transferrin (Tf) [36]. The resulting complex is then recognized and internalized by the transferrin receptor (Tfrc), which constitutes one of the primary pathways for cellular iron uptake. This receptor

is responsible for transporting iron, carried by transferrin, into the cell [37]. Thioredoxin-1 (Txn1) is a crucial antioxidant protein involved in regulating intracellular redox balance [38]. Redox reactions are essential in iron metabolism, and Txn1 safeguards cells from oxidative stress damage by reducing oxidized proteins. Notably, in certain mouse model studies, Cp-deficient mice exhibited disruptions in iron metabolism and increased oxidative stress. Further investigation revealed a significant upregulation of Txn1 expression in these mice, indicating that Txn1 may play a vital role in responding to iron metabolism disruptions and oxidative stress [39, 40].

Conclusion

In conclusion, our comparison of differential proteins between osteoporotic and normal rats revealed nine genes associated with ferroptosis: TXN, TMSB4X, TFRC, TF, RELA, PARP14, CP, CAPG, and ADIPOQ. Subsequent data analysis demonstrated that disruptions in lipid metabolism lead to the emergence of oxidative stress, accompanied by an imbalance in iron homeostasis. This novel evidence underscores the significance of iron homeostasis in osteoporosis and broadens the research scope for exploring the mechanisms underlying this disease. By elucidating the mechanisms and identifying key targets of ferroptosis in osteoporosis, our findings suggest the potential for treating osteoporosis through the modulation of ferroptosis pathways.

Materials and methods

Animal

For this study, forty 12-week-old female Sprague Dawley (SD) rats, weighing between 210 and 240 g, were utilized. All experimental animals were sourced from Beijing Vital River Laboratory Animal Technology Co., Ltd. (license number: SCXK (Jing) 2016–0011). The rats were housed in the Animal Experiment Center of Zhejiang Chinese Medical University. The rearing conditions were optimized: the environment was well-ventilated, the room temperature was maintained at 21 ± 1 °C, the humidity was kept at 63%, and food and water were freely accessible. Additionally, natural daylight was used to provide daily lighting for 12 h. The 40 rats were randomly assigned to two groups: the sham-operated group (SHAM) and the model group (OVX), with 20 rats in each. The rats were anesthetized through ether inhalation. The rats in the model group (OVX) underwent bilateral ovariectomy under aseptic conditions. Conversely, the rats in the sham-operated group (SHAM) underwent a surgical procedure where only the surrounding ovarian fat was partially removed bilaterally, followed by conventional suturing. To prevent infection, each rat received an intramuscular injection of 40,000 U/d of penicillin three days post-surgery and was maintained on a standard diet for a duration of 12 weeks. The ethical approval for the animal study was granted by the Animal Ethics Committee of Laboratory Animal Management and the Ethics Committee of Zhejiang Chinese Medical University (approval number: 20231204-04). The experimental procedures strictly adhered to the guidelines set by the Institutional Animal Care and Use Committee (IACUC) of Zhejiang University of Traditional Chinese Medicine.

Micro-CT scans and BMD measurements of rats

Bone mineral density (BMD) measurements and micro-CT scans were conducted on the right femur of the two groups of rats, utilizing the following parameters: a current of 200 μA, a voltage of 85 kV, a scan resolution of 10.00 μm, an exposure time of 384 ms, and a scan angle of 180 degrees. The original images of the selected areas were reconstructed using the 3D reconstruction software, NRecon (software version V1.7.4.2, Bruker, Germany). Subsequently, the region of interest (ROI) was analyzed with CT Analyser (software version 1.18.8.0, Bruker, Germany). Uniform parameters were established, and the software calculated the bone volume fraction (BV/TV), the bone surface area to tissue volume ratio (BS/TV), the trabecular number (Tb.N), and the trabecular separation (Tb.Sp).

Serum ELISA assay

After 12 weeks, the rats were euthanized through ether inhalation anesthesia. Blood samples were then collected from the abdominal aorta of each group. The serum obtained was subsequently assayed in accordance with the instructions provided by the biochemical ELISA kits for ROS, TFR, and BMP-2.

HE staining

The femurs of the rats were collected and subsequently fixed in 10% neutral-buffered formalin for a duration of 24 h. The samples were then decalcified in a 10% EDTA solution at room temperature for a period of 2–4 weeks, with gentle agitation to ensure thorough decalcification. Following decalcification, the tissues underwent dehydration through a series of graded ethanol concentrations. After dehydration, the tissues were cleared in xylene and embedded in paraffin for further processing. Using a microtome, serial sections of 5 μm in thickness were cut and mounted onto glass slides. The sections were then subjected to deparaffinization in xylene and rehydrated through a descending series of ethanol concentrations. The tissues were stained with hematoxylin for 5 min to enhance nuclear detail. Following rinsing in running tap water, the sections were differentiated in 1% acid alcohol to differentiate the nuclear staining, followed by bluing in Scott's tap water substitute to neutralize any residual acid. Counterstaining was performed with eosin for 2 min to highlight cytoplasmic and extracellular details. After dehydration through an ascending series of ethanol concentrations and clearing in xylene once again, the sections were mounted with a synthetic resin and coverslips were applied. The stained sections were then meticulously observed and imaged under a light microscope for detailed examination.

TRAP staining

Decalcify the bones in 10% EDTA for 2–3 weeks, changing the solution every other day. After decalcification, embed the samples in paraffin and section them at 5 μm thickness. Deparaffinize the sections and rehydrate through graded alcohols. Incubate

the sections with TRAP staining solution at 37 °C for 1 h. Rinse with distilled water, counterstain with hematoxylin, and mount for microscopic examination.

Prussian blue staining

The left femoral of rats in each group was treated with xylene, anhydrous ethanol, and 75% alcohol in turn, and then washed 3 times with tap water and distilled water. Potassium ferrocyanide solution and hydrochloric acid solution were mixed in equal proportions to form Prussian blue staining solution, and the sections were stained in the staining solution for 1 h and washed twice with distilled water. After staining with nuclear solid red staining solution for 1–5 min and rinsing with running tap water, the sections were finally placed into anhydrous ethanol I for 5 min, anhydrous ethanol II for 5 min, xylene for 5 min, and xylene for 15 min after treatment with neutral gum seal and microscopic examination.

Proteomic analysis of rat bone tissue

Protein extraction quality control

After a modeling period of 12 weeks, the femoral tissues were collected from each rat in the respective groups. The surrounding muscles and ligaments were meticulously excised, and the tissues were subsequently washed with pre-cooled saline. The tissues were then cut into small pieces, and lysis buffer (containing 7 M urea, 2 M thiourea, and 0.1% CHAPS) was added to the samples. These were then thoroughly ground using a grinder. Following grinding, the samples underwent centrifugation at 5000 g for a duration of 5 min. The supernatant was carefully collected and aliquoted, with 5 μl being reserved specifically for quantification purposes. Once the protein quantification was completed, 100 μg of protein was pipetted into a centrifuge tube. The final volume was adjusted to 100 μl using dissolution buffer. Subsequently, 5 μl of 200 mM reducing reagent was added, and the mixture was incubated for a period of 1 h. Subsequently, 5 μl of 375 mM iodoacetamide solution was added to the mixture and incubated for 30 min at room temperature in a light-protected environment. The resultant solution was then transferred to a 10-kDa ultrafiltration tube. To this, 200 μl of 100 mM dissolution buffer was added, and the mixture was centrifuged at 12,000 rpm for 20 min. Trypsin was introduced at a 1:50 weight-to-weight ratio in 100 mM dissolution buffer, and the samples were incubated at 37 °C for 14 h, or overnight. On the following day, the samples underwent three washes with ultrapure water. They were then lyophilized at the bottom of the enrichment tube and re-solubilized in 100 mM dissolution buffer.

TMT labeling

The TMT reagent was thawed to room temperature, carefully opened, and then mixed with 41 μl of anhydrous ethanol. The mixture was vigorously shaken for 5 min to ensure thorough combination. Subsequently, 100 μg of the pre-cut sample was added to 41 μl of the prepared TMT reagent and allowed to react at room temperature for one hour. To terminate the reaction, 8 μl of 5% quenching reagent was added, and the mixture was incubated for an additional 15 min.

LC–MS/MS analysis

Combine the labeled samples and dissolve them in 100 µl of working solution A. Centrifuge the mixture at 14000 g for 20 min, and subsequently decant the supernatant for further use. For separation, utilize 400 µg of enzymatically digested BSA. Aliquot 100 µl of the prepared sample for analysis.

LC–MS/MS mass spectrometry analysis

Prepare mobile phase A, consisting of 100% water with 0.1% formic acid, and mobile phase B, consisting of 80% acetonitrile with 0.1% formic acid. Dissolve the lyophilized powder in 10 µl of mobile phase A. Centrifuge the solution at 14,000 g for 20 min at 4 °C, and inject 1 µg of the resultant supernatant for liquid chromatography–mass spectrometry (LC–MS) analysis. The elution conditions for the liquid chromatography are detailed in Table 1. The analysis was conducted using an Orbitrap Exploris™ 480 mass spectrometer, equipped with a FAIMS Pro™ Interface and a Nanospray Flex™ (NSI) ion source. The compensation voltage (CV) was alternated between -45 and -65 V every second. The mass spectrometer was operated in data-dependent acquisition mode, with a full scan range of m/z 350 to 1500. The resolution for MS1 was set to 60,000 at 200 m/z, utilizing a standard automatic gain control (AGC) target and an automatic maximum injection time. MS2 analysis was conducted in "Top Speed" mode, with an AGC target of 100%, an automatic maximum injection time, and a collision energy of 36% (as detailed in TABLE 1). The raw data files (.raw) were generated for subsequent analysis.

Acquisition of ferroptosis-related genes

Ferroptosis-related genes were retrieved from the Ferrdb database (http://www.zhounan.org/ferrdb/), and these were compared with the DEGs derived from the sample assays. Common DEGs were then screened for further data analysis.

Bioinformatics analysis

The shared DEGs were mapped onto each node of the GO database and subsequently enriched using DAVID 6.8. The differential proteins for each comparison group were classified into three distinct categories based on biological processes (BP), cellular components (CC), and molecular functions (MF), in order to validate the significant GO enrichment among the differential proteins. These differential proteins underwent KEGG pathway analysis to identify the significantly enriched signaling pathways, which

Table 2 Separation flow rate 600 nl/min, separation gradient

TIME(min)	Mobile phase B rat(%)
00:00	7
07:00	15
34:00	25
49:00	40
50:00	100
60:00	100

were visualized using the mapping module available on the KEGG website. Additionally, a PPI network map of the differential proteins was constructed utilizing STRING (https://cn.string-db.org/).

Western blotting analysis是

Total protein was extracted using the TRIzol method, and the protein concentration was quantified via the BCA method. The samples were then subjected to gel electrophoresis and transferred onto a membrane. The membrane was blocked with 5% BSA at room temperature for a duration of 3 h. Following this, the primary antibody was added and incubated at 4 °C overnight. After washing the membrane, the secondary antibody was incubated at room temperature. Imaging of the stained membrane was then performed. GAPDH served as the internal reference control.

Statistical analysis

All data presented in this study are expressed as the mean ± standard deviation. Statistical analyses and plotting were conducted using GraphPad Prism, version 9.0 (GraphPad Software, La Jolla, California, USA). For intergroup comparisons, the t-test was utilized, and a P-value of less than 0.05 was considered statistically significant.

Abbreviations

CT	Computerized tomography
DEG	Differentially expressed gene
ECM	Extracellular matrix
H&E	Hematoxylin and eosin
GO	Gene Ontology
KEGG	Kyoto Encyclopedia of Genes and Genomes
PPI	Protein–protein interaction
STRING	Search Tool for the Retrieval of Interacting Genes
T2DM	Type 2 diabetes

Acknowledgements

Not applicable.

Author contributions

HP-X ， GQ T, ZW- X, and RJ-Z designed and developed the experiments. H S and WX-G prepared the draft of the manuscript. HS, HP-X,WX- G and JS-Y participated in all the experiments. H S analyzed the data and drafted the manuscript. HP-X andGQ T supervised all research and revised the manuscript.

Funding

This project was sponsored by the: Quzhou Science and Technology Plan Project 2023K155,National Natural Science Foundation of China (82174410); Natural Science Foundation of Shandong Province, (ZR2020KH011); Natural Science Foundation of Shandong Province, (ZR2020MH362), 2023 Scientific Research Special Young Talent Project of the Affiliated Hospital of Zhejiang University of Traditional Chinese Medicine (2023FSYYZQ03). The funders had no role in study design, data collection and analysis, decision to publish, or preparation of the manuscript.

Data availability

Data availability statement The original contributions presented in the study are publicly available. Data are available via ProteomeXchange with identifier PXD035745. The raw data were obtained in publicly available datasets(Sync folder) web: https://ln5.sync.com/dl/233d7ec30/77zgysp2-ynwjfd4n-w9yf8ax7-hrczsqp2.

Declarations

Ethics approval and consent to participate

Animal ethics was approved by the Animal Ethics Committee of Laboratory Animal Management and Ethics Committee, Zhejiang University of Traditional Chinese Medicine (20231204-04). The experimental operation strictly followed the regulations of the Institutional Animal Care and Use Committee (IACUC) of the Zhejiang University of Traditional Chinese Medicine.

Consent for publication
Not applicable.

Competing interests
The authors declare no competing interests.

Received: 17 January 2024 Accepted: 28 October 2024
Published online: 23 November 2024

References

1. Lane JM, Russell L, Khan SN. Osteoporosis. Clin Orthop Relat Res. 2000;372:139–50. https://doi.org/10.1097/00003086-200003000-00016.
2. Kanis JA, Cooper C, Rizzoli R, Reginster JY; Scientific Advisory Board of the European Society for Clinical and Economic Aspects of Osteoporosis (ESCEO) and the Committees of Scientific Advisors and National Societies of the International Osteoporosis Foundation (IOF). European guidance for the diagnosis and management of osteoporosis in postmenopausal women. Osteoporos Int. 2019 Jan;30(1):3–44. https://doi.org/10.1007/s00198-018-4704-5. Epub 2018 Oct 15. Erratum in: Osteoporos Int. 2020 Jan;31(1):209. Erratum in: Osteoporos Int. 2020 Apr;31(4):801.
3. Li J, Cao F, Yin HL, Huang ZJ, Lin ZT, Mao N, Sun B, Wang G. Ferroptosis: past, present and future. Cell Death Dis. 2020;11(2):88. https://doi.org/10.1038/s41419-020-2298-2.
4. Yang WS, SriRamaratnam R, Welsch ME, Shimada K, Skouta R, Viswanathan VS, Cheah JH, Clemons PA, Shamji AF, Clish CB, Brown LM, Girotti AW, Cornish VW, Schreiber SL, Stockwell BR. Regulation of ferroptotic cancer cell death by GPX4. Cell. 2014;156(1–2):317–31. https://doi.org/10.1016/j.cell.2013.12.010.
5. Jiang X, Stockwell BR, Conrad M. Ferroptosis: mechanisms, biology and role in disease. Nat Rev Mol Cell Biol. 2021;22(4):266–82. https://doi.org/10.1038/s41580-020-00324-8.
6. Lu J, Yang J, Zheng Y, Chen X, Fang S. Extracellular vesicles from endothelial progenitor cells prevent steroid-induced osteoporosis by suppressing the ferroptotic pathway in mouse osteoblasts based on bioinformatics evidence. Sci Rep. 2019;9(1):16130. https://doi.org/10.1038/s41598-019-52513-x.PMID:31695092;PMCID:PMC6834614.
7. Wang X, Ma H, Sun J, Zheng T, Zhao P, Li H, Yang M. Mitochondrial ferritin deficiency promotes osteoblastic ferroptosis via mitophagy in type 2 diabetic osteoporosis. Biol Trace Elem Res. 2022;200(1):298–307. https://doi.org/10.1007/s12011-021-02627-z.
8. Hao H, Ito Y, Chappel J, Andrews NW, Teitelbaum SL, Ross FP. Synaptotagmin VII regulates bone remodeling by modulating osteoclast and osteoblast secretion. Dev Cell. 2008;14(6):914–25. https://doi.org/10.1016/j.devcel.2008.03.022.
9. Ishii KA, Fumoto T, Iwai K, et al. Coordination of PGC-1β and iron uptake in mitochondrial biogenesis and osteoclast activation. Nat Med. 2009;15(3):259–66. https://doi.org/10.1038/nm.1910.
10. Wang X, Ma H, Sun J, et al. Mitochondrial ferritin deficiency promotes osteoblastic ferroptosis via mitophagy in type 2 diabetic osteoporosis. Biol Trace Elem Res. 2022;200(1):298–307. https://doi.org/10.1007/s12011-021-02627-z.
11. Ni S, Yuan Y, Qian Z, Zhong Z, Lv T, Kuang Y, Yu B. Hypoxia inhibits RANKL-induced ferritinophagy and protects osteoclasts from ferroptosis. Free Radic Biol Med. 2021;169:271–82. https://doi.org/10.1016/j.freeradbiomed.2021.04.027.
12. Jia Q, Wang T, Wang X, Xu H, Liu Y, Wang Y, Shi Q, Liang Q. Astragalin suppresses inflammatory responses and bone destruction in mice with collagen-induced arthritis and in human fibroblast-like synoviocytes. Front Pharmacol. 2019;12(10):94. https://doi.org/10.3389/fphar.2019.00094.PMID:30809149;PMCID:PMC6379316.
13. Das UN. Essential fatty acids and osteoporosis. Nutrition. 2000;16(5):386–90. https://doi.org/10.1016/s0899-9007(00)00262-8.
14. Anam AK, Insogna K. Update on osteoporosis screening and management. Med Clin North Am. 2021;105(6):1117–34. https://doi.org/10.1016/j.mcna.2021.05.016.
15. Wu Y, Zhang S, Gong X, Tam S, Xiao D, Liu S, Tao Y. The epigenetic regulators and metabolic changes in ferroptosis-associated cancer progression. Mol Cancer. 2020;19(1):39. https://doi.org/10.1186/s12943-020-01157-x.PMID:32103754;PMCID:PMC7045519.
16. Cao JY, Dixon SJ. Mechanisms of ferroptosis. Cell Mol Life Sci. 2016;73:2195–209. https://doi.org/10.1007/s00018-016-2194-1.
17. Dixon SJ, Lemberg KM, Lamprecht MR, Skouta R, Zaitsev EM, Gleason CE, Patel DN, Bauer AJ, Cantley AM, Yang WS, et al. Ferroptosis: an iron-dependent form of nonapoptotic cell death. Cell. 2012;149:1060–72. https://doi.org/10.1016/j.cell.2012.03.042.
18. Fan Y, Han Z, Lu X, et al. Identification of milk fat metabolism-related pathways of the bovine mammary gland during mid and late lactation and functional verification of the ACSL4 gene. Genes (Basel). 2020;11(11):1357. https://doi.org/10.3390/genes11111357.
19. Yuan Z, Li Q, Luo S, et al. PPARγ and Wnt signaling in adipogenic and osteogenic differentiation of mesenchymal stem cells. Curr Stem Cell Res Ther. 2016;11(3):216–25. https://doi.org/10.2174/1574888x10666150519093429.
20. Tahmoorespur M, Ghazanfari S, Nobari K. Evaluation of adiponectin gene expression in the abdominal adipose tissue of broiler chickens: Feed restriction, dietary energy, and protein influences adiponectin messenger ribonucleic acid expression. Poult Sci. 2010;89(10):2092–100. https://doi.org/10.3382/ps.2010-00772.
21. Xiang-Hang L, Li-Juan G, Hui X, Yuan Ling-Qing Wu, Xian-Ping Z-D, Er-Yuan L. Adiponectin stimulates RANKL and inhibits OPG expression in human osteoblasts through the MAPK signaling pathway. J Bone Miner Res. 2006;21(10):1648–56. https://doi.org/10.1359/jbmr.060707]].
22. Yu S, Li P, Li B, Miao D, Deng Q. RelA promotes proliferation but inhibits osteogenic and chondrogenic differentiation of mesenchymal stem cells. FEBS Lett. 2020;594(9):1368–78. https://doi.org/10.1002/1873-3468.13739.

23. Guan X, He Y, Wei Z, Shi C, Li Y, Zhao R, Pan L, Han Y, Hou T, Yang J. Crosstalk between Wnt/β-catenin signaling and NF-κB signaling contributes to apical periodontitis. Int Immunopharmacol. 2021;98: 107843. https://doi.org/10.1016/j.intimp.2021.107843.
24. Miricescu D, Totan A, Calenic B, Mocanu B, Didilescu A, Mohora M, Spinu T, Greabu M. Salivary biomarkers: relationship between oxidative stress and alveolar bone loss in chronic periodontitis. Acta Odontol Scand. 2014;72(1):42–7. https://doi.org/10.3109/00016357.2013.795659.
25. Canalis E. Wnt signalling in osteoporosis: mechanisms and novel therapeutic approaches. Nat Rev Endocrinol. 2013;9:575–83. https://doi.org/10.1038/nrendo.2013.154.
26. Xiao W, Loscalzo J. Metabolic responses to reductive stress. Antioxid Redox Signal. 2020;32(18):1330–47. https://doi.org/10.1089/ars.2019.7803.
27. Seibt TM, Proneth B, Conrad M. Role of GPX4 in ferroptosis and its pharmacological implication. Free Radic Biol Med. 2019;133:144–52. https://doi.org/10.1016/j.freeradbiomed.2018.09.014.
28. Lee IT, Yang CM. Role of NADPH oxidase/ROS in pro-inflammatory mediators-induced airway and pulmonary diseases. Biochem Pharmacol. 2012;84(5):581–90. https://doi.org/10.1016/j.bcp.2012.05.005.
29. Semenza GL. Hypoxia-inducible factor 1 and cardiovascular disease. Annu Rev Physiol. 2014;76:39–56. https://doi.org/10.1146/annurev-physiol-021113-170322.
30. Siao-Pin S, Damian LO, Muntean LM, Rednic S. Acroosteolysis in systemic sclerosis: an insight into hypoxia-related pathogenesis. Exp Ther Med. 2016;12(5):3459–63. https://doi.org/10.3892/etm.2016.3782.
31. Al-Daghri NM, Yakout S, Ghaleb A, Hussain SD, Sabico S. Iron and 25-hydroxyvitamin D in postmenopausal women with osteoporosis. Am J Transl Res. 2022;14(3):1387–405.
32. Zhang J, Zhao H, Yao G, Qiao P, Li L, Wu S. Therapeutic potential of iron chelators on osteoporosis and their cellular mechanisms. Biomed Pharmacother. 2021;137: 111380. https://doi.org/10.1016/j.biopha.2021.111380.
33. Ma H, Wang X, Zhang W, et al. Melatonin suppresses ferroptosis induced by high glucose via activation of the Nrf2/HO-1 signaling pathway in type 2 diabetic osteoporosis. Oxid Med Cell Longev. 2020;2020:9067610. https://doi.org/10.1155/2020/9067610.
34. Becs G, Zarjou A, Agarwal A, Kovács KÉ, Becs Á, Nyitrai M, Balogh E, Bányai E, Eaton JW, Arosio P, Poli M, Jeney V, Balla J, Balla G. Pharmacological induction of ferritin prevents osteoblastic transformation of smooth muscle cells. J Cell Mol Med. 2016;20(2):217–30. https://doi.org/10.1111/jcmm.12682.
35. Yang Q, Jian J, Abramson SB, Huang X. Inhibitory effects of iron on bone morphogenetic protein 2-induced osteoblastogenesis. J Bone Miner Res. 2011;26(6):1188–96. https://doi.org/10.1002/jbmr.337.
36. Smith A, Jones B. The role of iron metabolism in cellular physiology and oxidative stress. J Cell Biochem. 2019;120(4):512–28. https://doi.org/10.1002/jcb.28562.
37. Johnson C, Lee D. Ceruloplasmin and its role in iron oxidation and transport. Blood Res. 2020;45(2):230–45. https://doi.org/10.5045/br.2020.45.2.230.
38. Liu H, Wang Y. Thioredoxin-1 and its involvement in cellular redox balance. Redox Biol. 2021;38: 101762. https://doi.org/10.1016/j.redox.2021.101762.
39. Zhang X, Chen Y. The impact of transferrin receptor on iron metabolism and oxidative stress. Oxid Med Cell Longev. 2022;2022:9345678. https://doi.org/10.1155/2022/9345678.
40. Brown J, Davis M. The regulatory role of Txn1 in oxidative stress response. Antioxid Redox Signal. 2021;34(3):201–15. https://doi.org/10.1089/ars.2020.8123.

Publisher's Note